AIAA AVIATION Forum
June 27-July 1, 2022, Chicago, IL & Virtual
AIAA AVIATION 2022 Forum

10.2514/6.2022-3337

Check for updates

Evolutionary Algorithm applied to Differential Reynolds Stress Model for Turbulent Boundary Layer subjected to an Adverse Pressure Gradient

Erij Alaya*
German Aerospace Center (DLR), Institute of Aerodynamics and Flow Technology
Göttingen, lower Saxony, 37073, Germany

Cornelia Grabe†
German Aerospace Center (DLR), Institute of Aerodynamics and Flow Technology
Göttingen, lower Saxony, 37073, Germany

Bernhard Eisfeld‡
German Aerospace Center (DLR), Institute of Aerodynamics and Flow Technology
Braunschweig, lower Saxony, 38108, Germany

Downloaded by Markus Ruetten on December 6, 2022 | http://arc.aiaa.org | DOI: 10.2514/6.2022-3337

In this paper, an evolutionary algorithm is implemented for the purpose of performing symbolic regression in an attempt to improve Reynolds-Averaged-Navier-Stokes models predictions. In contrast to most machine learning algorithms, Gene Expression Programming generates a mathematical expression that can be directly interpreted and implemented into the Computational Fluid Dynamics solver. In this paper, the latter feature is exploited based on high-fidelity data to ascertain novel correlations for the pressure-strain correlation within a particular Differential Reynolds Stress Model, the Speziale-Sarkar-Gatski (SSG) model. The CFD-driven Gene Expression Programming is considered for the curved backward-facing step. Two models are obtained regarding the industrially relevant phenomenon of a turbulent boundary layer under adverse pressure gradient. The models are tested on a range of validation cases.

I. Nomenclature

a_{12}	=	Anisotropy ratio
b_{12}	=	Bradshaw constant
b_{ij}	=	Component of Reynolds stress anisotropy tensor
c_f	=	Skin friction coefficient
C_i	=	Coefficients of pressure-strain correlation

*C²A²S²E – Center for Computer Applications in AeroSpace Science and Engineering, erij.alaya@dlr.de
†C²A²S²E – Center for Computer Applications in AeroSpace Science and Engineering, cornelia.grabe@dlr.de
‡C²A²S²E – Center for Computer Applications in AeroSpace Science and Engineering, deceased January 2022

Copyright © 2022 by German Aerospace Center (DLR). Published by the American Institute of Aeronautics and Astronautics, Inc., with permission.

C_{ij} = Component of Reynolds stress convection, m^2/s^3

c_p = Pressure coefficient

C_μ = Equilibrium parameter

D_{ij} = Component of Reynolds stress diffusion, m^2/s^3

F_1 = Blending function by Menter

h = Genome head length

H = Step height, m

I_b = First invariant of Reynolds stress anisotropy tensor

II_b = Second invariant of Reynolds stress anisotropy tensor

II_S = Second invariant of strain rate tensor

$\widetilde{II}_S$ = Normalized second invariant of strain rate tensor

III_b = Third invariant of Reynolds stress anisotropy tensor

$\widetilde{III}_b$ = Normalized third invariant of Reynolds stress anisotropy tensor

$\tilde{k}$ = Specific kinetic turbulence energy, m^2/s^2

L = Flat plate length, m

n = Number of arguments of a mathematical operator

P_{ij} = Component of Reynolds stress production, m^2/s^3

$\tilde{R}_{ij}$ = Component of specific Reynolds stress tensor, m^2/s^2

Re = Reynolds number

Re_t = Tubulent Reynolds number

$\widetilde{Re}_t$ = Normalized tubulent Reynolds number

$\tilde{S}_{ij}$ = Component of mean strain rate tensor, $1/s$

$\tilde{S^*}_{ij}$ = Component of traceless strain rate tensor, $1/s$

t = Genome tail length

u = Streamwise velocity, m/s

u^+ = Non-dimensional velocity in inner scaling

u'' = Component of fluctuating velocity, m/s

U_i = Velocity component, m/s

U_{in} = Inlet streamwise velocity, m/s

$u'u'^+$ = Non-dimensional Reynolds streamwise stress in inner scaling

$u'v'^+$ = Non-dimensional Reynolds shear stress in inner scaling

v'' = Component of fluctuating velocity, m/s

Downloaded by Markus Ruetten on December 6, 2022 | http://arc.aiaa.org | DOI: 10.2514/6.2022-3337

$v'v'^{+}$ = Non-dimensional Reynolds wall-normal stress in inner scaling

w'' = Component of fluctuating velocity, m/s

$\tilde{W}_{ij}$ = Component of mean rotation tensor, $1/s$

$w'w'^{+}$ = Non-dimensional Reynolds spanwise stress in inner scaling

x = streamwise cartesian coordinate, m

y = wall-normal cartesian coordinate, m

y^{+} = Non-dimensional wall distance in inner scaling

symbols

α_ω = Coefficient of ω-production

β_ω = Coefficient of ω-destruction

δ_{ij} = Kronecker symbol

ϵ = Dissipation rate, m^2/s^3

ϵ_{ij} = Component of Reynolds stress dissipation, m^2/s^3

$\mathscr{F}$ = Function set

$\mathfrak{I}$ = Input data set

θ = Momentum thickness, m

Θ = Value predicted by GEP

$\hat{\Theta}$ = Target value

κ = Von-Kármán constant

μ = Dynamic viscosity, $kg/(ms)$

Π_{ij} = Component of pressure-strain correlation, m^2/s^3

$\bar{\rho}$ = Density, kg/m^3

σ_d = Coefficient of cross-diffusion

σ_ω = Coefficient of ω-diffusion

$\Phi^{(\epsilon)}$ = Coefficient belonging to ϵ-equation

$\Phi^{(\omega)}$ = Coefficient belonging to ω-equation

ω = Specific dissipation rate, $1/s$

Downloaded by Markus Ruetten on December 6, 2022 | http://arc.aiaa.org | DOI: 10.2514/6.2022-3337

II. Introduction

The field of Computational Fluid Dynamics (CFD) has grown significantly in the past decades thanks to the substantial increase in capacities of modern computers. In particular, Reynolds-Averaged-Navier-Stokes (RANS) calculations have become a standard in today's industrial applications yielding good accuracy at low-cost when compared to very expensive high-fidelity simulations like Direct Numerical Simulation (DNS) and Large Eddy Simulation (LES). However, RANS calculations rely completely on turbulence models, which are prone to errors especially when predicting complex flows e.g. separated flows [1].

While state-of-the-art RANS turbulence models deliver reliable results in many cases, certain industrially relevant flow phenomena remain challenging. One of these flow phenomena is the Turbulent Boundary Layer (TBL) subjected to an Adverse Pressure Gradient (APG) on a smooth surface, which is of significant importance for many engineering applications. Ongoing effort is being made to improve RANS models using classical methods to better understand these flow phenomena [2] [3] [4]. Although considerable progress has been achieved in this field, the development has stagnated [5] [6]. For this reason, an increasing effort is made to introduce machine learning (ML) to turbulence modeling as a novel method to generate more accurate, data-driven turbulence models. The rapidly growing number of publications covering the application of ML techniques to turbulence modeling [7] [8] shows the expected potential of ML in identifying new, previously unexplored correlations in closure models. Some of the popular data-driven turbulence modeling approaches are the field inversion and machine learning approach of Duraisamy et al. [9] [10], the physics-informed machine learning for turbulence modeling of Ling et al. [11] [12] [13] and the Gene Expression Programming (GEP) of Weatheritt and Sandberg [14]. The latter approach is used in this paper because, unlike most ML Neural-Network based methods, it provides insights into the derived relations by generating tangible and interpretable mathematical expressions instead of a black-box ML model. Yielding these expressions allows verifying the physical plausibility of the model and the direct implementation into a CFD solver. For example, in a series of published papers [15][16][17][18], Weatheritt et al. made a continuous effort to further develop the GEP tool to expand the Boussinesq approximation within Menter's Shear Stress Transport model [19].

While most publications cover ML-methods for eddy-viscosity based RANS turbulence models, the application of ML to Differential Reynolds Stress models (DRSM) is still an open field of research. DRSM models are considered the most advanced RANS turbulence models. By solving six transport equations for the Reynolds stress components [20] plus one length-scale equation [21][22][23], these models are in principle capable of predicting the interaction between Reynolds stresses and mean velocity gradients more comprehensively [24], and, therefore, are more attractive to be applied for complex 3D flows [25][26][23]. In DRSM, the production of the Reynolds stresses is exactly given [25], however, the transport equations for the Reynolds stress tensor contain further unknown terms, e.g. the pressure-strain correlation needs to be modeled and therefore include uncertainty. Hence, the purpose of the present work is to apply

Downloaded by Markus Ruetten on December 6, 2022 | http://arc.aiaa.org | DOI: 10.2514/6.2022-3337

the GEP approach to DRSM in an attempt to improve its prediction for TBL under APG with and without separation. The presented work is part of the HORIZON2020 project HiFi-TURB, where high-fidelity DNS data for several key flow phenomena are generated and interrogated using machine learning techniques to extract information to improve advanced state-of-the-art RANS turbulence models.

This paper starts with an introduction into GEP. Afterwards, the details about applying GEP to a DRSM model, the Speziale-Sarkar-Gatski (SSG) model [27] and the flow features considered by the GEP algorithm are presented. GEP training for the curved backward-facing step test case [28] [29] resulted in two models, which are then tested on multiple cases.

Downloaded by Markus Ruetten on December 6, 2022 | http://arc.aiaa.org | DOI: 10.2514/6.2022-3337

III. Methodology

A. The GEP approach

Gene Expression Programming (GEP) is an evolutionary algorithm first introduced by Ferreira [30] in 2001. It is a genotype-phenotype algorithm that uses concepts of biology and modern genetics and is based on the Darwinian evolutionary theory "survival of the fittest" [31]. This section is based primarily on the work of Ferreira [30], Zhong et al. [32] and Weatheritt [33]. As any evolutionary algorithm, the basic concept of GEP is summed up in the following figure:

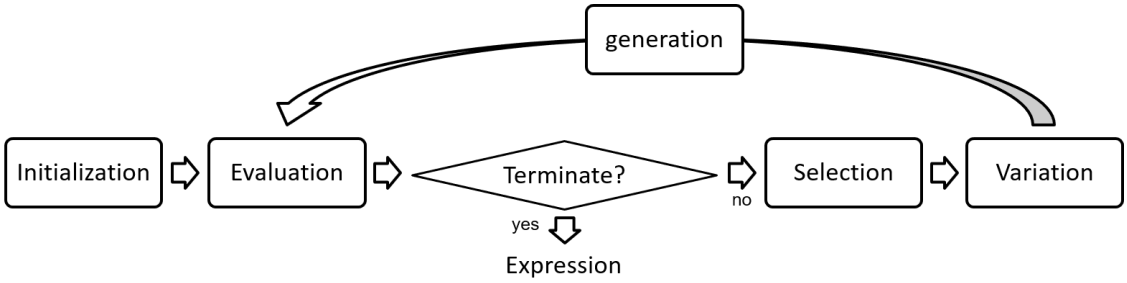

Fig. 1 GEP basic concept

Initially, the GEP tool starts by creating a population of candidates (also called individuals, organisms or chromosomes). The creation of these individuals is a random process and does not undergo any constraints. Each individual is encoded in a fixed-length string of arbitrary linked genes called genotype, which stores the entire genetic information that can be evolved. The genotype encloses the so-called phenotype, which constitutes the functional expression of the individual. The phenotype can be represented as an expression tree, which can vary in size, despite the fixed-length nature of the genotype. To ensure the constant correct representation of the phenotype, the genotype is encoded as a head of predefined length h that contains an input set of arguments e.g. $\mathfrak{I} = \{a, b\}$ as well as a function

set of mathematical operators, e.g. $\mathcal{F} = \{+, -, \times, \cos\}$ and a tail that only contains input arguments with the length $t = h(n-1)+1$ where n represents the number of arguments the mathematical operator with the most arguments takes. As an example, we take the genotype illustrated in Fig. 2 as string representation.

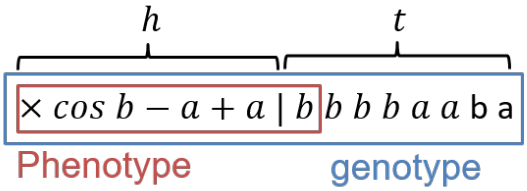

Fig. 2 GEP individual: String representation

The head and the tail are separated by the symbol "|". As depicted in Fig. 2, the head contains elements of the input set as well as from the function set, whereas the tail only contains elements from the input set. This is to ensure that every mathematical operator contains a sufficient number of input arguments. In this example, there are two types of mathematical operators: the one that can take one single argument like the cosine function cos and the others that require two arguments like the addition or the multiplication function. This means the maximal number of arguments that can be processed by a mathematical operator in this example is $n = 2$. With the head length being set to 7, we can determine the tail length $t = 7 \times (2-1)+1 = 8$. As mentioned before, the phenotype, in this case "$\cos(b) \times (a-(a+b))$", can be represented by a tree structure as in Fig. 3.

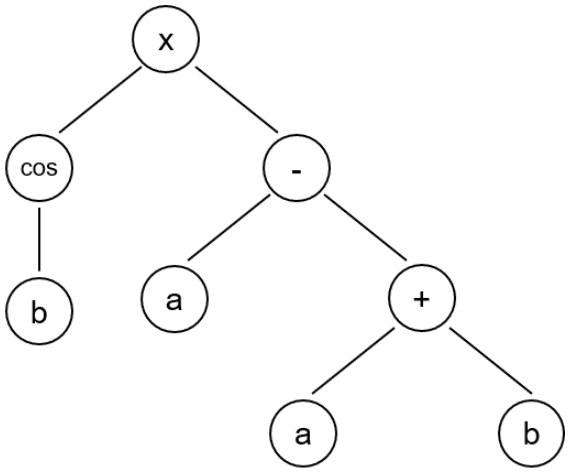

Fig. 3 GEP individual: Expression tree representation

In this fashion, GEP combines the advantages of a string structure in being versatile and simple to manipulate and the tree structure in being easy to grasp. Further details of the working mechanisms of GEP can be found in [30], [33] and [14].

Downloaded by Markus Ruetten on December 6, 2022 | http://arc.aiaa.org | DOI: 10.2514/6.2022-3337

The next step is the evaluation of the fitness of the populations' individuals. For every individual, the cost function, which is selected depending on the application, is calculated. In this paper, the basic mean-square-error MSE is selected:

$$\text{cost function} = E((\Theta - \hat{\Theta})^2) \tag{1}$$

where Θ represents the value predicted by the GEP tool and $\hat{\Theta}$ represents the value considered as "truth". At this point, the individuals performing well (low-cost function) are kept, and the ones that perform poorly are forced to die out. The evaluation produced is then transported further to the termination step, where each individuals' performance is assessed by termination criteria. There are three termination criteria:

- One of the individuals performs very well and the goal is thereby achieved
- The number of generations has reached the maximum set by the user
- There is a performance stagnation and the individuals are not presenting an obvious improvement

If one of them is met, the computation stops immediately and the individual with the best fitness is rendered. However, if the termination criterion is unmet, the computation moves on to the selection step. Selection means, in this context, natural selection, where a mechanism is put in place in which the "fittest" individuals are picked out and can act as "parents" in the subsequent steps allowing them to pass their genetic information to a following generation. The selection methods (mostly roulette wheel selection or tournament selection) include some randomness, with the fittest individuals having the highest chance at getting picked out. The variation step introduces modifications to the selected individuals using genetic operations. These variations include crossover, mutation, reproduction, replication, etc. Ultimately, the generation of a new population takes place by looping through the last four steps until one of the termination criteria is met.

B. Application of GEP approach to Differential Reynolds Stress Models

1. RSM model equations

The GEP approach has already been used successfully in turbulence modeling for Explicit-Algebraic Reynolds Stress Models (EARSM) by Weatheritt and Sandberg et al. [14]. The GEP tool, EVE3 [14], that was developed and deployed for the purpose, is used in this work to explore its potential in improving the prediction of Differential Reynolds Stress Models (DRSM) for a selected flow phenomenon. For this purpose, a detailed examination of the DRSM model is carried out. In this section a brief description of the exact Reynolds transport equation and its components, followed by the modeling methodology of the Speziale-Sarkar-Gatski (SSG) model [27] and finally the application of the GEP tool on the model is presented.

The exact Reynolds Stress Transport equation describes the evolution of individual components of the Reynolds

Downloaded by Markus Ruetten on December 6, 2022 | http://arc.aiaa.org | DOI: 10.2514/6.2022-3337

stress tensor [34]:

$$\frac{\partial \bar{\rho}\tilde{R}_{ij}}{\partial t} + \frac{\partial}{\partial x_k}\bar{\rho}\tilde{R}_{ij}\tilde{U}_k = \bar{\rho}P_{ij} + \bar{\rho}\Pi_{ij} - \bar{\rho}\epsilon_{ij} + \bar{\rho}D_{ij} \tag{2}$$

where P_{ij} is the production term, Π_{ij} is the pressure-strain correlation term , ϵ_{ij} is the dissipation term and D_{ij} is the diffusion term. $\bar{\rho}\tilde{R}_{ij} = \overline{\rho u_i'' u_j''}$ are the specific Reynolds stresses with the corresponding non-dimensional anisotropies:

$$b_{ij} = \frac{\tilde{R}_{ij}}{2\tilde{k}} - \frac{1}{3}\delta_{ij} \tag{3}$$

The anisotropy invariants are:

$$I_b = b_{ii} = 0 \qquad II_b = -\frac{1}{2}b_{ij}b_{ij} \qquad III_b = \frac{1}{3}b_{ij}b_{jk}b_{ki} \tag{4}$$

The production term P_{ij} and the pressure-strain correlation term Π_{ij} are considered to have the same order of magnitude and are of substantial importance in most engineering relevant flows [24]. While the production term is closed and given exactly, the pressure-strain correlation involves essentially unmeasurable correlations [24] and requires modeling. In incompressible and weakly compressible flows, it is responsible for distributing turbulent kinetic energy among the components of the Reynolds stresses [34]. The exact expression of the pressure-strain correlation is:

$$\bar{\rho}\Pi_{ij} = \overline{p'\left(\frac{\partial u_i''}{\partial x_j} + \frac{\partial u_j''}{\partial x_i}\right)} \tag{5}$$

Multiple models for the pressure-strain correlation exist. The most general ones are by Lumeley and Newman [35] as well as by Johansson and Hallbäck[36] [37]. The SSG model is a widely used turbulence model which is based on a quadratic equation and is utilized throughout this work. It is given by

$$\begin{aligned}\bar{\rho}\Pi_{ij} = &-\left(C_1\bar{\rho}\epsilon + \frac{1}{2}C_1^*\bar{\rho}P_{kk}\right)\tilde{b}_{ij} + C_2\bar{\rho}\epsilon\left(\tilde{b}_{ik}\tilde{b}_{kj} - \frac{1}{3}\tilde{b}_{kl}\tilde{b}_{lk}\delta_{ij}\right)\\ &+\left(C_3 - C_3^*\sqrt{\tilde{b}_{kl}\tilde{b}_{kl}}\right)\bar{\rho}\tilde{k}\tilde{S}_{ij}^* + C_4\bar{\rho}\tilde{k}\left(\tilde{b}_{ik}\tilde{S}_{jk} + \tilde{b}_{jk}\tilde{S}_{ik} - \frac{2}{3}\tilde{b}_{kl}\tilde{S}_{kl}\delta_{ij}\right)\\ &+C_5\bar{\rho}\tilde{k}\left(\tilde{b}_{ik}\tilde{W}_{jk} + \tilde{b}_{jk}\tilde{W}_{ik}\right)\end{aligned} \tag{6}$$

where:

Table 1 SSG model constants

C_1	C_1^*	C_2	C_3	C_3^*	C_4	C_5
3.4	1.8	4.2	0.8	1.3	1.25	0.4

Downloaded by Markus Ruetten on December 6, 2022 | http://arc.aiaa.org | DOI: 10.2514/6.2022-3337

The calibrated constants in Tab.1 are believed to be functions of the anisotropy invariants listed in eq.(4) [24]. In this paper, an attempt is made to extract mathematical expressions from the GEP tool, with which the constants C_i in the SSG model are replaced. In addition to the anisotropy invariants II_b and III_b as potential dependencies, the second invariant of the strain rate tensor tenor II_S (eq.(7)) and the turbulent Reynolds number Re_t (eq.(8)) are also considered in the training process with:

$$II_S = \frac{1}{C_\mu \omega}\sqrt{\tilde{S^*_{ij}}\tilde{S^*_{ij}}} \quad ; \qquad \tilde{S^*_{ij}} = \tilde{S_{ij}} - \frac{1}{3}\tilde{S_{kk}}\delta_{ij} \tag{7}$$

$$\mathrm{Re_t} = \frac{\rho \tilde{k}}{\mu C_\mu \omega} \tag{8}$$

These five input parameters have different orders of magnitude in the flow phenomenon investigated, which increases the probability of some parameters getting excluded during the training process. As a preventive measure, a normalization is applied and the following five parameters are considered for the GEP training process:

$$II_b \qquad \sqrt{II_b} \qquad \widetilde{III}_b = \frac{III_b}{III_b + 1} \qquad \widetilde{II}_S = \frac{II_S}{II_S + 1} \qquad \widetilde{\mathrm{Re_t}} = \frac{\mathrm{Re_t}}{\mathrm{Re_t} + 1} \tag{9}$$

The number of constant coefficients in eq.(6) exceeds the number of Reynolds stress anisotropies in two-dimensional flow at turbulent equilibrium. As a result, different sets of coefficients can yield various similar solutions [37]. Hence, there is no unique solution and the problem is over-determined. Adding the fact that, with seven different coefficients to optimize, the search domain is extensive, the GEP training process becomes challenging.

Furthermore, most DRSM models are calibrated by turbulent equilibrium flows. As a result, separated flow regions are often overestimated [25][38] [39]. This has been shown by Eisfeld in [25] where the author also stated that no DRSM model with fixed coefficients would be able to predict all flow phenomena accurately. Hence, in this work we are not claiming to identify one model that would deliver an accurate solution for every flow phenomenon but, rather, a model that shows an improvement in the case of turbulent boundary layers subjected to an adverse pressure gradient including separation. In the best case scenario, this would not have a detrimental effect on the prediction of other flow phenomena or turbulent equilibrium flows, like the turbulent boundary layer for the zero-pressure gradient flat plate.

Note that, although the original SSG model [27] is based on the length scale variable ϵ, Menter's baseline ω-equation, which is based on the specific dissipation rate ω, is used in this work to supply the length scale variable. As mentioned by Eisfeld in [37], this helps avoid the need for any additional near-wall treatment.

$$\frac{\partial \bar{\rho}\omega}{\partial t} + \frac{\partial}{\partial x_k}\bar{\rho}\omega\tilde{U}_k = \alpha_\omega \frac{\omega}{\tilde{k}}\frac{\bar{\rho}P_{kk}}{2} - \beta_\omega \bar{\rho}\omega^2 + \frac{\partial}{\partial x_k}\left[\left(\bar{\mu} + \sigma_\omega \frac{\bar{\rho}\tilde{k}}{\omega}\right)\frac{\partial \omega}{\partial x_k}\right] + \sigma_d \frac{\bar{\rho}}{\omega} max\left(\frac{\partial \tilde{k}}{\partial x_j}\frac{\partial \omega}{\partial x_j}, 0\right) \tag{10}$$

Downloaded by Markus Ruetten on December 6, 2022 | http://arc.aiaa.org | DOI: 10.2514/6.2022-3337

In the length scale equation eq.(10), the coefficients $\phi = \alpha_\omega, \beta_\omega, \sigma_\omega, \sigma_d$ are blended by applying Menter's F_1 function (see Tab.2):

$$\Phi = F_1 \Phi^{(\omega)} + (1 - F_1)\Phi^{(\epsilon)} \tag{11}$$

with the superscript ω representing the near wall region and the superscript ϵ the outer region of Menter's baseline equation [40] [41] [42].

Table 2 Menter's baseline ω-equation coefficients

	α_ω	β_ω	σ_ω	σ_d
near wall (ω)	0.5556	0.075	0.5	0
outer region (ϵ)	0.44	0.0828	0.856	1.712

In this work, the production and destruction terms of the near wall region as well as the outer region ($\alpha_\omega^{(\omega)}, \alpha_\omega^{(\epsilon)}, \beta_\omega^{(\omega)} and\ \beta_\omega^{(\epsilon)}$) are further calibrated by the GEP method to investigate their influence on a GEP-modified DRSM model.

2. GEP approach application

There are two possibilities of applying the GEP approach: frozen and CFD-driven [17]. In the frozen approach, RANS data is extracted from an existing CFD simulation and fed into the GEP tool as input data $\mathfrak{I}$ together with the function set $\mathscr{F}$ (see Fig. 4). In this case, the GEP tool generates a set of candidates for the pressure-strain correlation Π_{ij}^{GEP} which is then evaluated against the high-fidelity data Π_{ij}^{HiFi}, considered as "truth", by means of a cost function (see eq. (1)). The RANS data remain the same during the process of generating new expressions for the pressure-strain correlation term, thus the term "frozen" [17]. The final selection for the pressure-strain correlation term is implemented into the CFD-code for an evaluation.

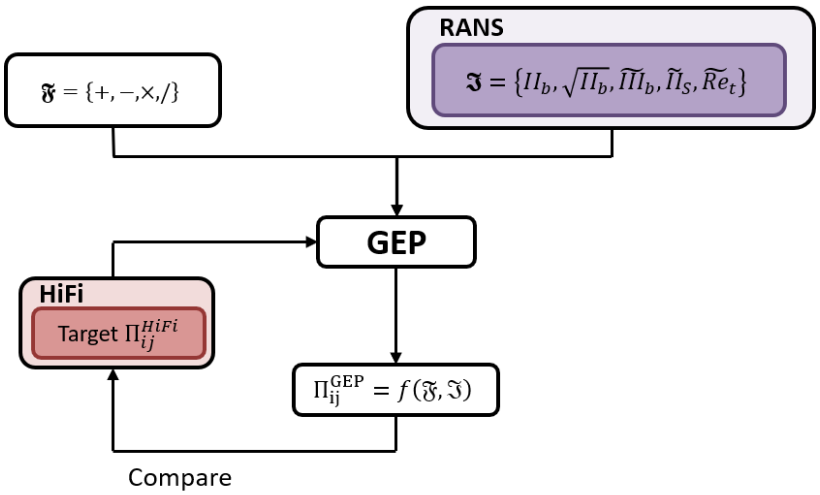

Fig. 4 GEP frozen approach

Downloaded by Markus Ruetten on December 6, 2022 | http://arc.aiaa.org | DOI: 10.2514/6.2022-3337

The frozen method is a good choice when using input data that is independent of the parameter being altered. This is not the case for the pressure-strain correlation Π_{ij} where the flow field variables, including anisotropy invariants, are dependent on the coefficients of the pressure-strain correlation. When the coefficients are adjusted by the GEP tool also the flow field and the pressure-strain correlation changes. As this influence on the flow solution is not considered in the frozen approach, it is difficult to quantify the improvement made by the GEP tool, which makes the selection process prone to errors.

Furthermore, modifying only the pressure-strain correlation does not automatically imply an improved flow field prediction. Hence, a reliable evaluation process should be based on a quantity directly linked to the flow phenomenon to be predicted. The frozen GEP method has been investigated extensively in a preliminary step of this work. Although some models that were extracted from the frozen process showed improvement in the training process, not all models converged when implemented into the CFD solver and even fewer yielded an improved prediction compared to the original SSG model.

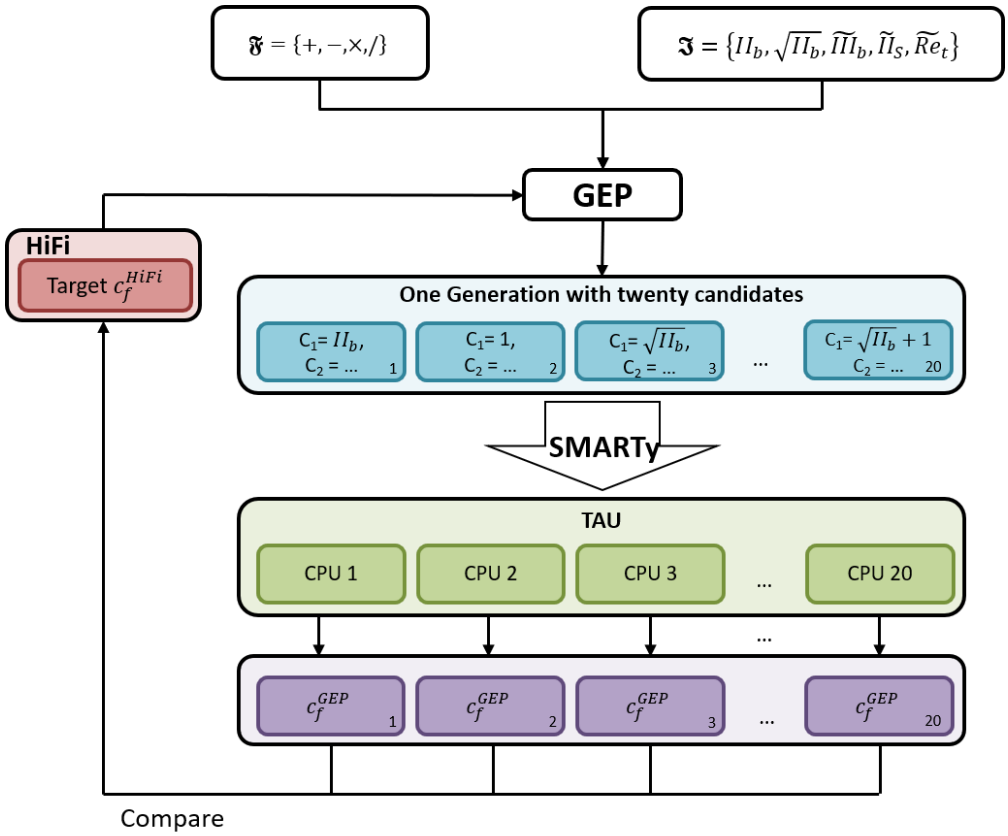

Fig. 5 GEP CFD-driven approach

To overcome the shortcomings of the frozen GEP method in this particular case, the CFD-driven approach is introduced [17] (see Fig.5). During this process, the GEP tool is assigned a function set $\mathfrak{F}$ just as in the frozen approach. However, unlike the frozen approach, the input set $\mathfrak{I}$ serves only as a placeholder for the following steps. The GEP tool

Downloaded by Markus Ruetten on December 6, 2022 | http://arc.aiaa.org | DOI: 10.2514/6.2022-3337

then generates a set of candidates as a random mix of function set and input set parameters. In Fig.5, the number of generated candidates in one generation is 20, which is the case for all the models presented in the following sections of the paper. Here, each individual in the pool of candidates is implemented into the CFD-code and a RANS simulation is performed. Depending on the solution of the computations, the performance of the individual candidates is evaluated based on a selected informative quantity.

The focus of this work is mainly on separated flow and, in particular, the accurate prediction of the separation region (separation point, reattachment point and bubble shape). An appropriate measure for the separation region is the skin friction coefficient c_f. While the pressure-strain correlation Π_{ij} is still being modified by replacing each coefficient C_i with a GEP produced expression, the evaluation of the GEP produced expression is not based on the pressure-strain correlation. Instead, the individual candidates are automatically implemented into individual versions of the CFD-code, which are then compiled. From the results of the individual CFD computations performed simultaneously, each c_f^{GEP} is compared separately to the skin friction coefficient c_f^{HiFi} from a high-fidelity data set using the cost funtion in eq.(1). Besides the goal-oriented evaluation of an expression by an informative quantity (the skin friction coefficient), the evaluation also accounts for numerical robustness, as candidates with poor convergence will be not considered in an upcoming generation. The process is repeated as displayed in Fig.1 until a termination criterion is met.

Downloaded by Markus Ruetten on December 6, 2022 | http://arc.aiaa.org | DOI: 10.2514/6.2022-3337

C. Numerical method

All CFD simulations were performed using the DLR in-house software TAU [43]. TAU is an unstructured cell-centered on dual-grids code of $2^{nd}-$order accuracy. For the computations performed here, the mean-flow and turbulence convective terms are discretized using $2^{nd}-$order upwind schemes together with Matrix Dissipation. Low-Mach number preconditioning was applied and steady computations using a LU-SGS scheme were performed. All results presented in this report are based on fully converged simulations.

DLR's SMARTy toolbox [44], which is a modular, object-oriented python package, is used as a framework for implementing the candidate function derived by GEP in TAU and extracting computational information .

The GEP framework EVE* (Evolutionary algorithm for the development of Expressions)[14] used in this work is a Python based tool that symbolically regresses algebraic expressions built on GEP concepts.

IV. Results

A. GEP Models for the Curved Backward-Facing Step

For the GEP training, the curved backward-facing step ("CS test case") of Bentaleb et al.[28] and Lardeau et al.[29] was selected. The flow phenomenon studied is a turbulent boundary layer subjected to an adverse pressure gradient. High-fidelity data from LES simulations are available on the NASA-TMR Website [45]. It is a 2D test case with a

*provided by Prof. Richard Sandberg, University of Melbourne

Reynolds number of Re = 13700 based on the step height H including a separation in the step area. The LES data for this test case are from a grid with 23.6 million grid cells. The RANS computations are conducted using a hybrid mesh with a grid cell count of 42730 (see Fig.6). For the inlet boundary condition, LES data were used to set a velocity profile inlet boundary condition.

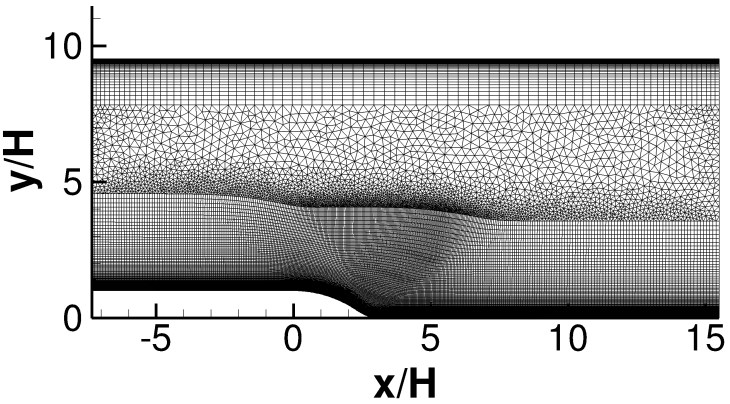

Fig. 6 CS test case: Geometry and mesh

The test case contains several local flow types which cannot be predicted correctly with one set of coefficients for the pressure-strain term of the SSG model [37]. Although the area of interest is the separated flow region, an improvement there should not deteriorate the prediction accuracy of other flow areas or other basic test cases. Therefore, the training process considers the complete flow field including the zero-pressure gradient (ZPG) regions, the adverse pressure gradient (APG) zone and the separation zone. The skin friction coefficient c_f is the target quantity for the model optimization. The skin friction distribution for the CS test case (see Fig.7a) rapidly changes in the reattachment area and in the area where the separation starts. This yields an increased sensitivity of the cost function in these two areas. Thus, the skin friction coefficient is a well suited quantity for the optimization process, considering that the accurate prediction of these two areas is the focus of this work.

As already stated, the first CFD-driven GEP training includes the pressure-strain correlation coefficients C_i, only. With seven different coefficients to optimize, the GEP tool is facing an extensive search pool. From a preliminary study, it appeared that the coefficient C_2 does not have a major apparent influence on the skin friction coefficient c_f. For this reason, it was excluded from in the first CFD-driven GEP training. This leaves six coefficients to be optimized ($C_1, C_1^*, C_3, C_3^*, C_4$ and C_5). The complexity of the expressions was kept minimal to increase the probability of numerical convergence. The outcome of the GEP training heavily relies on the initial population, which is created randomly. For this reason, multiple initial populations were generated until satisfactory results were achieved. A second CFD-driven GEP training was performed using the model from the first training process as a starting point. In the second process, C_2 was trained as a function of the same input data as the other coefficients C_i. In addition, four parameters of the length-scale equation ($\alpha_\omega^{(\omega)}, \alpha_\omega^{(\epsilon)}, \beta_\omega^{(\omega)} and\ \ \beta_\omega^{(\epsilon)}$) were optimized as constants with no parameter

Downloaded by Markus Ruetten on December 6, 2022 | http://arc.aiaa.org | DOI: 10.2514/6.2022-3337

dependency. Two promising models (SSGGEP-mod1 and SSGGEP-mod2) resulted from these two training processes and the new coefficients are listed in Tab.3 and Tab.4 together with the coefficients of the original model. Note that these models are solely presented as a proof-of-concept of the GEP method and are not recommended to be used as an established turbulence model.

Table 3 Comparison of coefficients for the pressure-strain correlation

Model version	C_1	C_1^*	C_2	C_3	C_3^*	C_4	C_5
SSG original	3.4	1.8	4.2	0.8	1.3	1.25	0.4
SSGGEP-mod1	$(\widetilde{II}_S/0.066)+2$	1.0	$\widetilde{III}_b$	$-59.301\widetilde{Re}_t$	0.312	0.112	-0.158
SSGGEP-mod2	$(\widetilde{II}_S/0.066)+2$	1.0	2.0	$-59.301\widetilde{Re}_t$	0.312	0.112	-0.158

Table 4 Comparison of coefficients for the length-scale equation

Model version	$\alpha_\omega^{(\omega)}$	$\alpha_\omega^{(\epsilon)}$	$\beta_\omega^{(\omega)}$	$\beta_\omega^{(\epsilon)}$
SSG original	0.556	0.44	0.075	0.0828
SSGGEP-mod1	0.475	0.5	0.0675	0.095
SSGGEP-mod2	0.75	0.55	0.095	0.095

Note that, the absence of some input parameters from the SSGGEP models presented does not reflect their relevance. Other models with very similar training results included other of the five input parameters. As stated previously, there is no unique solution and different sets of coefficients can lead to a very similar result.

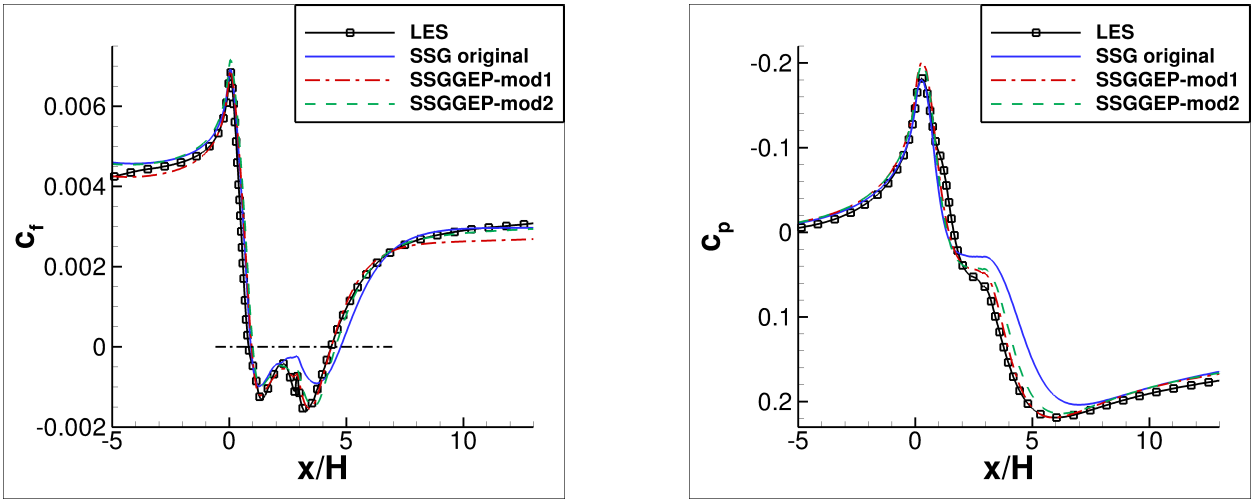

(a) skin friction coefficient c_f **(b) pressure coefficient c_p**

Fig. 7 CS test case: skin friction coefficient and pressure coefficient

The CS LES data alongside the results of the SSG original model and the two modified models (SSGGEP-mod1 and SSGGEP-mod2) are presented in Fig. 7 to Fig.9. Overall, the new models show an improvement in comparison to the

Downloaded by Markus Ruetten on December 6, 2022 | http://arc.aiaa.org | DOI: 10.2514/6.2022-3337

original SSG model. For the skin friction coefficient c_f, which was the target value during the training process, the first model SSGGEP-mod1 yields a better agreement with the LES data in the separation region. However, upstream and downstream of the separation area, SSGGEP-mod1 predicts a slightly decreased value of the skin friction coefficient, which indicates an overall decreased shear stress in the ZPG region. This is expected to affect the results for basic flow types, where the original model performs well. The SSGGEP-mod2 model delivers a better prediction of the skin friction coefficient downstream of the reattachment point and very similar results to the SSG original model upstream of the separation region, but still has a better agreement with the LES reference data across the separation region in comparison to the original model. Both models underestimate the pressure gradient close to the separation point but present an improved agreement in the pressure coefficient c_p across the separation region, with the SSGGEP-mod1 yielding slightly better results than SSGGEP-mod2.

Table 5 lists the separation and reattachment point for the reference LES data, the original SSG model and the two modified models. Although the original model presents a slightly better agreement in the separation point with the reference LES data in comparison with the two modified models, both GEP models show a much better recovery than the original SSG model with SSGGEP-mod2 predicting a slightly slower recovery than SSGGEP-mod1.

Table 5 CS test case: separation and reattachment points (x/H)

	LES	SSG original	SSGGEP-mod1	SSGGEP-mod2
separation point	0.828373	0.924192	0.953797	1.004217
reattachement point	4.354517	4.759437	4.361017	4.543052

The previous statements are confirmed by the qualitative comparison of the shape of the separated region indicated by the velocity streamlines in Fig.8. Both SSGGEP models yield a separation bubble shape and size that are closer to the reference LES computation in comparison to the original SSG model.

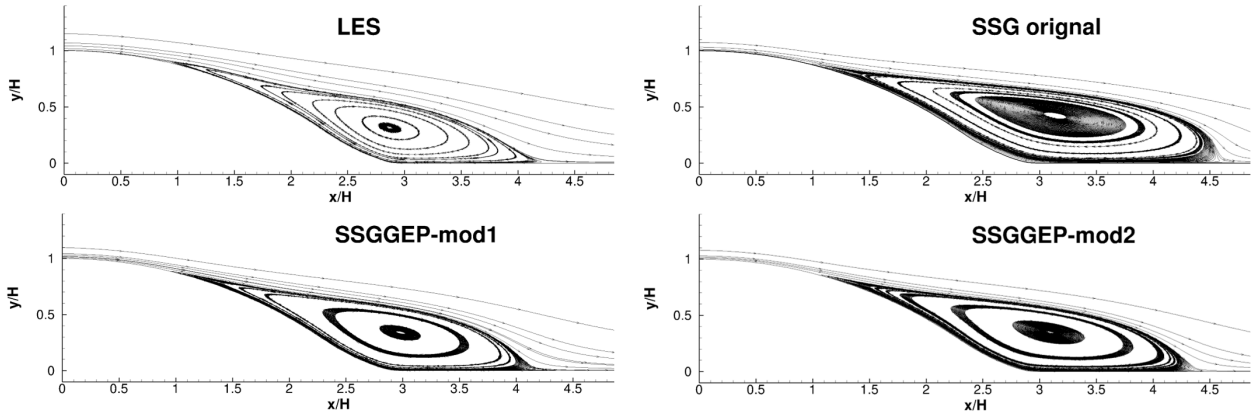

Fig. 8 CS test case: shape of separated region

Downloaded by Markus Ruetten on December 6, 2022 | http://arc.aiaa.org | DOI: 10.2514/6.2022-3337

Note that although the target quantity c_f is a surface parameter, the improvements delivered by the GEP training are not limited to the skin friction coefficient c_f. In agreement with the qualitative results shown in Fig. 8, the velocity profiles displayed in Fig.9 fit the LES data quite well.

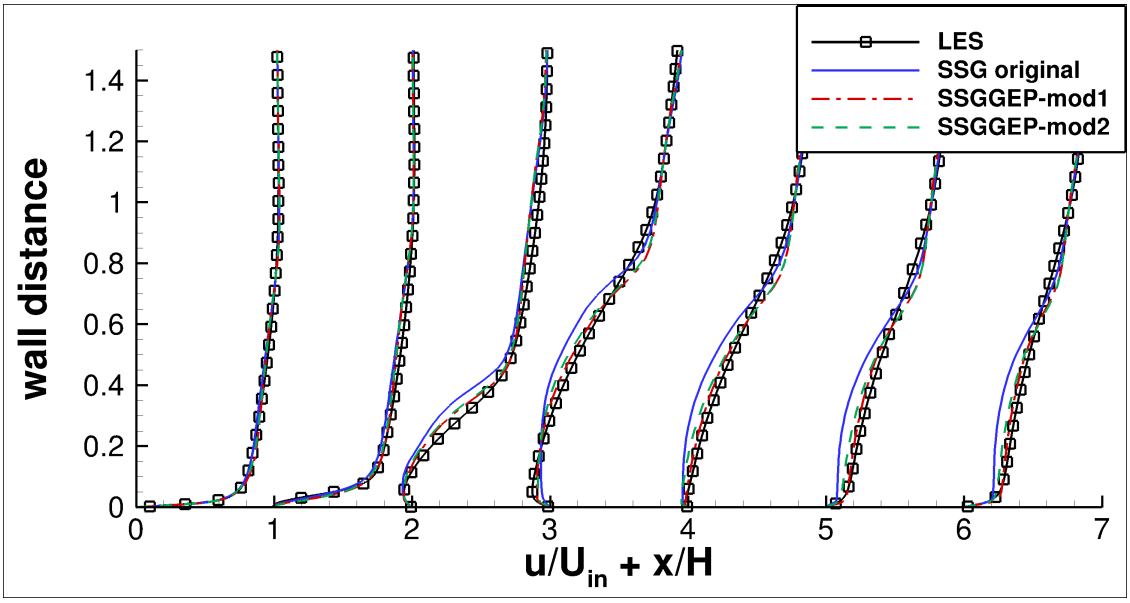

Fig. 9 CS test case: streamwise velocity profiles u/U_{in} over separation area

In the following section, the SSGGEP models are tested against the SSG original model for other test cases.

B. Validation cases

In this section, the SSGGEP models are tested against two standard cases: the turbulent flat plate at zero pressure gradient and the channel flow. Additionally, results of a newly designed test case are presented.

1. Flat plate

The flat plate boundary layer at zero pressure gradient is a standard computational case against which, every turbulence model should be tested. Thus, computational results are presented here for a flat plate at ZPG with a Reynolds number $Re_L = 14 \times 10^6$ based on the flat plate length L. The aim of this study is to account for the influence of the modified models over an equilibrium state flow. The computations were carried out on the finest grid, with 545×385 grid points, provided on the NASA-TMR website [46] and were conducted for SSG original model as well as the SSGGEP models. The results are then compared to the DNS data of Schlatter [47].

Fig.10a shows the skin friction distribution c_f over the local Reynolds number Re_θ based on the momentum thickness θ. The behavior of the skin friction distribution reflects the results obtained for the curved backward-facing step in Fig.7a. As expected, SSGGEP-mod1 underestimates the skin friction, whereas, SSGGEP-mod2 demonstrates a very similar behavior compared to the SSG original model for low Re_θ values and a slightly steeper decrease in c_f for

Downloaded by Markus Ruetten on December 6, 2022 | http://arc.aiaa.org | DOI: 10.2514/6.2022-3337

higher values of Re_θ, thus yielding better agreement with the DNS data. Consistent with the skin friction distribution results, mean velocity profile in inner scaling at $Re_\theta = 2000$ are shown in Fig.10b. In the viscous sublayer, all three RANS models coincide and are in good agreement with the DNS data. In the buffer layer, the SSGGEP-mod1 is in good agreement with the DNS reference data whereas the SSGGEP-mod2 model conforms with the original SSG model until it parts ways with it in the log-law region and outer region which results in a better agreement with the DNS reference Data. However, by overestimating the mean velocity, SSGGEP-mod1 does not perform well in the latter two regions.

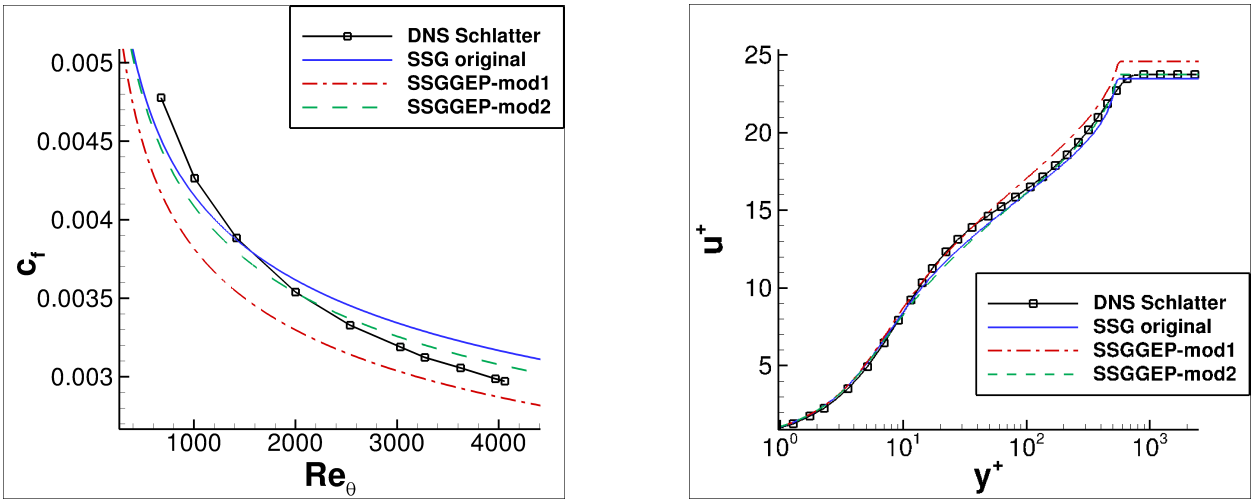

(a) skin friction coefficient c_f

(b) mean velocity profile for $Re_\theta = 2000$

Fig. 10 Flat plate: skin friction coefficient and velocity profile

Fig.11 illustrates the Reynolds stresses normalized by the friction velocity u_τ at a local Reynolds number $Re_\theta = 2000$. For the Reynolds normal stress components $u'u'^+$, $v'v'^+$ and $w'w'^+$ a striking similarity between the two modified models is immediately apparent. This can be attributed to the similarity in the pressure-strain correlation terms of the two models, which only differ in the coefficient C_2. As already stated, the pressure-strain correlation term is responsible for redistributing the turbulent kinetic energy among Reynolds stress components [34]. Any change in its coefficients yields a different redistribution. The consequence of the similar pressure-strain correlation of the SSGGEP models is a decrease in the Reynolds streamwise stress (Fig.11a) which is compensated by an increase of the Reynolds wall-normal stress and the Reynolds spanwise stress magnitude (Fig.11b and Fig.11c). Accordingly, the difference between the coefficients of the pressure-strain correlation of the original model and the ones of the modified models results in a different redistribution of the Reynolds stresses, as shown in Fig.11.

Unlike the Jakirlić-Hanjalić homogeneous (JHh) RSM model [48], which was especially designed to correctly predict near wall turbulence behavior, the SSG model is not particularly well adapted for this task [49]. This is reflected in the results of the Reynolds stresses in Fig.11. Therefore, the results are analyzed by mainly focusing on the log-law and outer regions ($y^+ > 200$). For $y^+ > 200$, the Reynolds normal stresses, except for the wall-normal component $v'v'^+$,

Downloaded by Markus Ruetten on December 6, 2022 | http://arc.aiaa.org | DOI: 10.2514/6.2022-3337

Downloaded by Markus Ruetten on December 6, 2022 | http://arc.aiaa.org | DOI: 10.2514/6.2022-3337

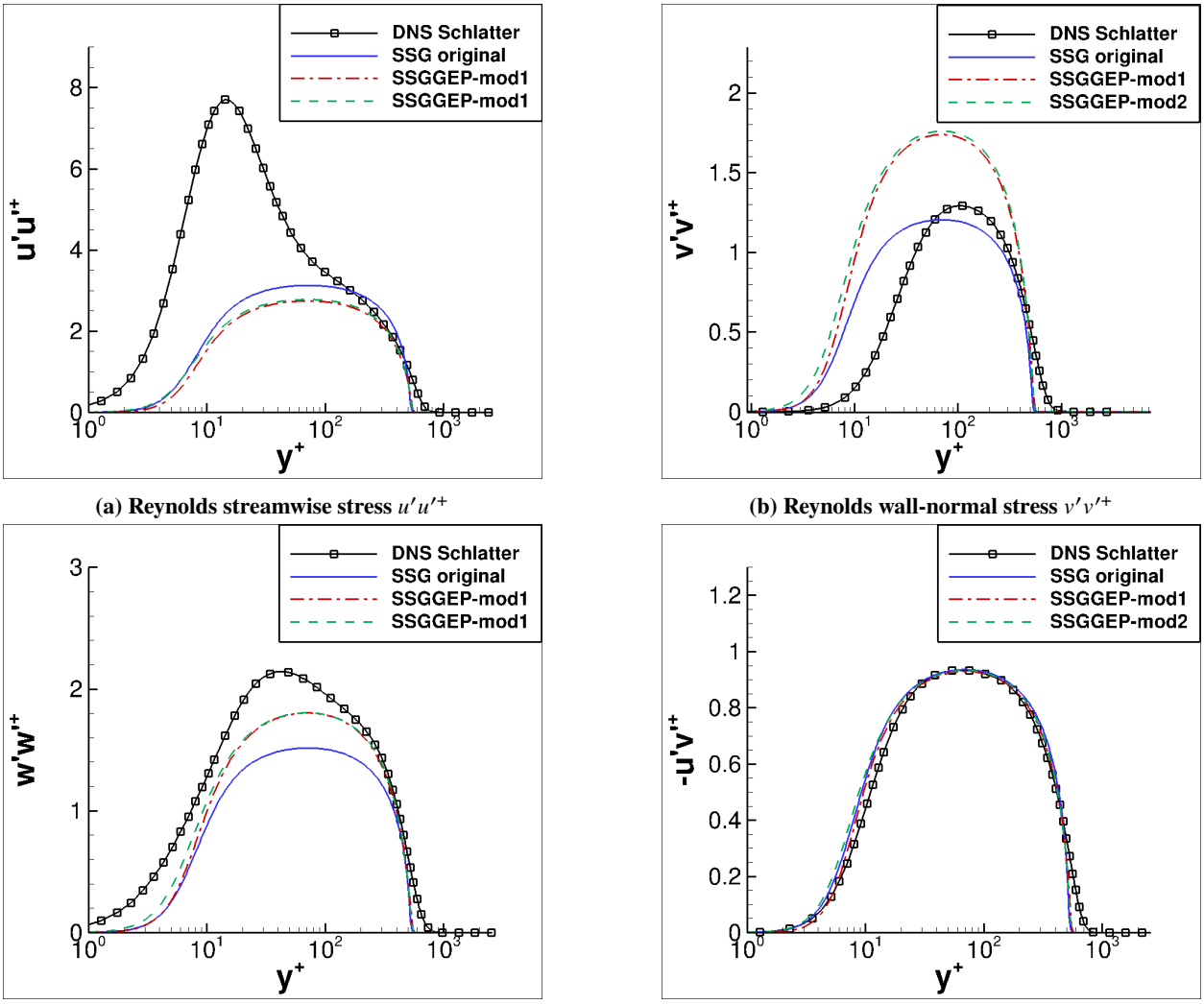

(a) Reynolds streamwise stress $u'u'^{+}$

(b) Reynolds wall-normal stress $v'v'^{+}$

(c) Reynolds spanwise stress $w'w'^{+}$

(d) Reynolds shear stress $u'v'^{+}$

Fig. 11 Flat plate: Reynolds stresses

of the SSGGEP-mod1 as well as SSGGEP-mod2 models are in a better agreement with the DNS reference data when compared to the original SSG model. Additionally, the dimensionless specific shear stress component $-u'v'^{+}$, plotted in Fig.11d over the dimensionless wall distance y^{+}, is in good agreement in magnitude and shape for all models with the reference DNS data with a slight improvement in the modified models over the original model for $y^{+} > 200$. Note that all models display the theoretical minimum of $-u'v'^{+} \approx 1$.

Depicted in Fig.12 is the anisotropy ratio $a_{12} = -u'v'/k$ which exhibits a plateau, from which the Bradshaw constant ($b_{12} = -a_{12}/2$) can be deduced. The Bradshaw hypothesis states that, independent of the pressure gradient, the value of b_{12} is constant over a wide wall-normal region and is equal to $b_{12} = -0.15$ [50]. For $y^{+} > 200$, the anisotropy constant value of the modified models is virtually identical to the DNS reference data and is aligned with the Bradshaw hypothesis, unlike the SSG original model. As shown in Fig.12, the two GEP models present an anomalie at the end of

the plateau where the anisotropy unexpectedly and briefly increases. This is potentially due to the modified values of the length-scale equation for the near wall and outer regions.

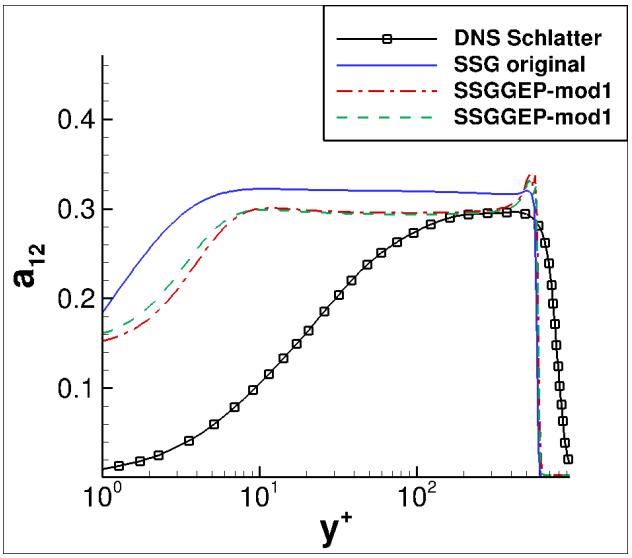

Fig. 12 Flat plate: anisotropy a_{12}

2. Channel flow

The channel flow is another standard validation test case in the turbulence modeling community. At a high Reynolds number of $Re_H = 80 \times 10^6$ based on the channel width H, this test case provides a pronounced logarithmic layer to be exploited for the analysis and evaluation of turbulence models. The computations were performed on the finest grid with 513×161 grid points available on the NASA-TMR Website [51]. The results are extracted from an axial position of $x = 500$ where it is assumed that fully developed turbulent flow conditions are achieved.

The mean velocity profile is depicted on Fig.13a for the original SSG model, SSGGEP-mod1 and SSGGEP-mod2 in addition to the theoretical log-law. Both modified models show an improvement over the original SSG model, with SSGGEP-mod2 exhibiting the closest match to the theoretical log-law.

Until recently, it was assumed that the von-Kármán constant κ takes a universal value between 0.4 and 0.41. However, in recent studies it was found that, depending on the flow type, the value can vary between 0.38 and 0.42 [52]. The von-Kármán constant κ can be deduced from Fig.13b, where the expression $d(\ln y^+)/du^+$ is plotted against the dimensionless wall distance y^+. The three models present a wide plateau for $10^2 < y^+ < 10^5$ where the expression is more or less constant with a maximum value that corresponds to κ. The original SSG model exhibits a value of 0.451 which is higher than the conventional range for κ, whereas SSGGEP-mod1 and SSGGEP-mod2 result in a value of 0.395 and 0.412 respectively, which is in good agreement with the experimentally measured value range.

Downloaded by Markus Ruetten on December 6, 2022 | http://arc.aiaa.org | DOI: 10.2514/6.2022-3337

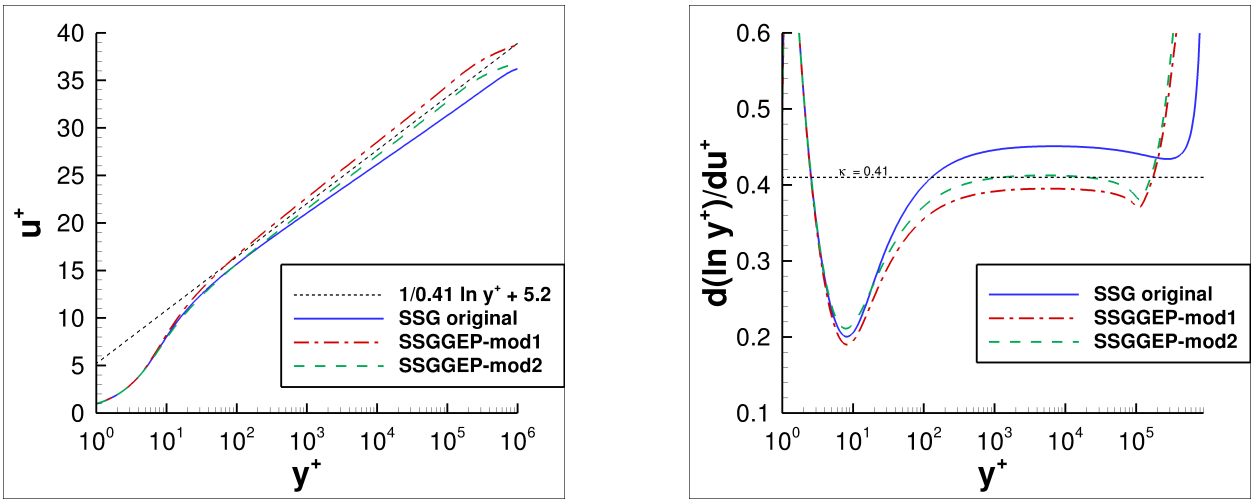

(a) mean velocity profile **(b) von-Kármán constant measure**

Fig. 13 Channel flow: mean velocity profile and von-Kármán constant measure

3. HiFi-TURB-DLR rounded step

The "HiFi-TURB-DLR rounded step" was designed in the framework of the European project HiFi-TURB [53] under grand agreement no 814837. The test case is designed to help investigate the effect of an adverse pressure gradient (APG) on a turbulent boundary layer (TBL). Planned DNS computations aim to provide comparison training data for the ML step. DNS calculations set limits on the Reynolds number as well as the general dimension of the viscous surface. This resulted in a 2D planar rounded step and a far-field boundary condition in the region opposite to the body wall (see Fig. 14). The geometry, which is based on the "Disotell"-test case of NASA [54], as well as the test case set-up is described in detail in [55].

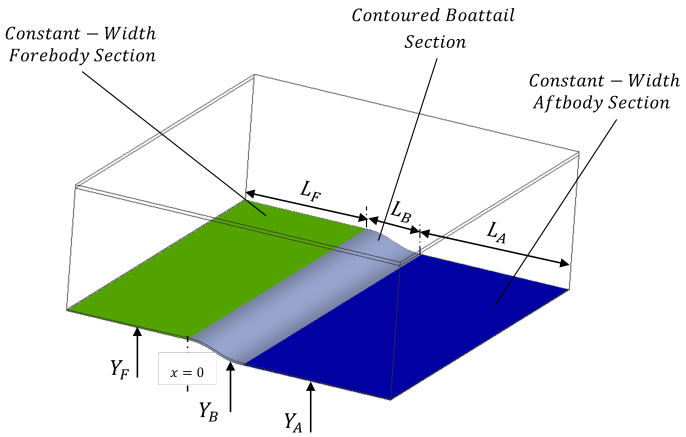

Fig. 14 HiFi-TURB DLR rounded step: set-up

Originally, the "HiFi-TURB-DLR rounded step" was designed specifically for the purpose of performing data-driven turbulence modeling based on the high-fidelity data generated within the project. Therefore, three different configurations

Downloaded by Markus Ruetten on December 6, 2022 | http://arc.aiaa.org | DOI: 10.2514/6.2022-3337

of the test case were designed to provide a parameter variation which is beneficial for the ML task. The configurations cover different levels of separation by modifying the step height obtaining: incipient separation, moderate separation and strong separation.

So far, DNS results of the HiFi-TURB-DLR rounded step are available only for the incipient configuration, where no separation occurs. The DNS computations were performed by project partners from the University of Bergamo (UniBg) for a Reynolds number of $Re = 549250$ based on the step height H. The grid for the DNS computations contains 15.01 million hexahedra with quadratic edges. Regarding RANS computations, a fully structured mesh with 266112 grid points was used.

The purpose of this validation test case is to test, if the results obtained during the training of the CS test case are also transmittable for a similar APG test case without an occurring separation. In Fig.15, the skin friction coefficient c_f as well as the pressure coefficient c_p are shown for all three models alongside the DNS results.

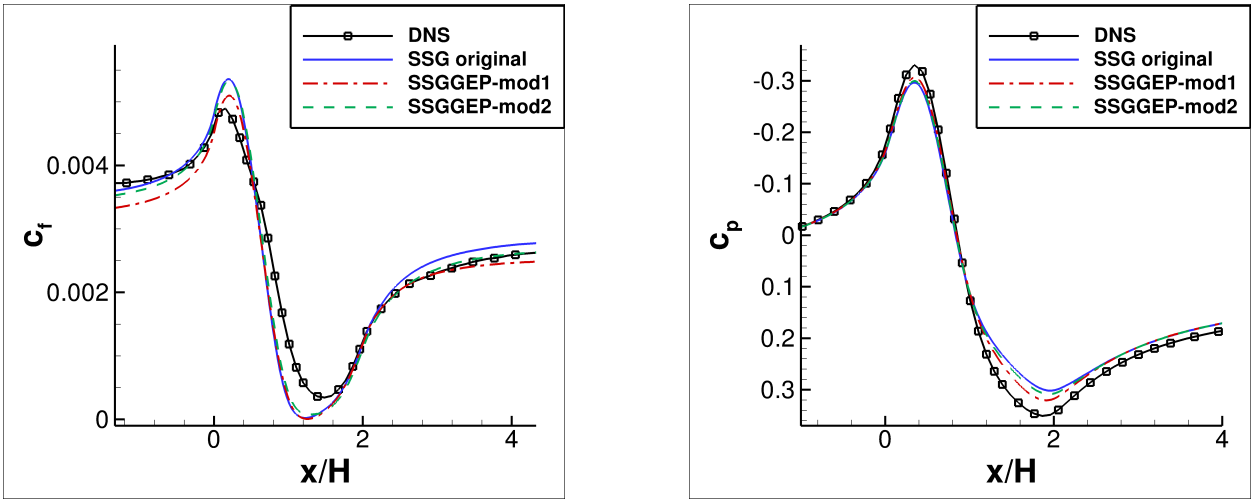

(a) skin friction coefficient c_f **(b) pressure coefficient c_p**

Fig. 15 HiFi-TURB-DLR rounded step: skin friction coefficient and pressure coefficient

In the region prior to the APG region, the behavior of the models is very similar to the CS test case: SSGGEP-mod1 exhibits an overall reduced skin friction distribution and the SSGGEP-mod2 model differs only slightly from the SSG original model. The reduced skin friction in SSGGEP-mod1 results in a smaller peak, better agreeing with the DNS data, whereas, SSGGEP-mod2 starts with a slightly reduced skin friction when compared to the original model, but demonstrates a similar peak. However, when the pressure gradient drops, SSGGEP-mod1 yields very similar results to the SSG original models, whereas the SSGGEP-mod2 model shows slight improvement near the minimum skin friction area and a subsequent match with DNS data in the recovery region (see Fig.15a). Concerning the pressure coefficient, Fig.15b demonstrates a consistent behavior of the models with SSGGEP-mod1 yielding the best agreement with the DNS data.

Downloaded by Markus Ruetten on December 6, 2022 | http://arc.aiaa.org | DOI: 10.2514/6.2022-3337

V. Summary and Outlook

The capabilities of an evolutionary algorithm were evaluated by improving the prediction of a Differential Reynolds Stress Model applied to a turbulent boundary layer subjected to an adverse pressure gradient with separation. During the training phase, the coefficients of the pressure-strain correlation term of the SSG model as well as some of the coefficients of the length-scale-supplying equation were modified. The training resulted in multiple models that showed improved predictions for the skin friction coefficient over the original SSG model for the curved backward-facing step. The results of two of these models have been presented in this paper. Subsequently, the models were tested for the turbulent flat plate, the channel flow and the HiFi-TURB-DLR rounded step, yielding promising results.

In the present work, purposefully, only the coefficients of the pressure-strain correlation model for the Reynolds stress transport equation as well as selected coefficients from the length-scale equation were taken into account by the GEP approach as it was decided to limit the training effort. However, other modeled terms exist, e.g. the diffusion term in the Reynolds stress transport equations. By evaluating candidate expressions by means of the skin friction coefficient, the coefficients modified during the training process compensate for all errors resulting from the original model. Additionally, other parameters used in this work were determined to fixed values including the number of individuals per generation, the termination criterion for the cost function and the number and scaling of input parameters as well as the input parameters themselves. This clearly shows that there is a need for systematic parameter studies as well as a more general feature (or input parameter) selection process. Next steps also include training on several turbulent boundary layers subjected to an adverse pressure gradients of varying strength as well as on reference data with higher-fidelity, e.g. the DNS results from the three configurations of the HiFi-TURB-DLR rounded step. Although using the skin friction coefficient as the only target value for model improvements proved to be quite effective, the use of a multi-objective approach [56] has the potential to further improve the results. Finally, in addition to the standard basic test cases, the models should be tested for more complex flows like the NASA Juncture Flow Model [57].

Downloaded by Markus Ruetten on December 6, 2022 | http://arc.aiaa.org | DOI: 10.2514/6.2022-3337

Acknowledgments

This work is part of the European Project HiFi-TURB which has received funding from the European Union's Horizon 2020 research and innovation programme under grant agreement No 814837. The authors gratefully acknowledge Prof. Richard Sandberg and Fabian Waschkowski of the University of Melbourne for providing us with the GEP interface, our project partners Alessandro Colombo and Francesco Carlo Massa for providing the DNS data for the HiFi-TURB-DLR rounded step test case and our colleague Tobias Knopp for his valuable comments.

Downloaded by Markus Ruetten on December 6, 2022 | http://arc.aiaa.org | DOI: 10.2514/6.2022-3337

References

[1] Bush, R. H., Chyczewski, T. S., Duraisamy, K., Eisfeld, B., Rumsey, C. L., and Smith, B. R., "Recommendations for Future Efforts in RANS Modeling and Simulation," *AIAA Scitech 2019 Forum*, American Institute of Aeronautics and Astronautics, 2019. https://doi.org/10.2514/6.2019-0317, URL https://doi.org/10.2514/6.2019-0317.

[2] Knopp, T., Buchmann, N. A., Schanz, D., Cierpka, C., Hain, R., Schröder, A., and Kähler, C. J., "Investigation of the Law-of-the-Wall for a Turbulent Boundary Layer Flow Subject to an Adverse Pressure Gradient Using Particle Imaging," *Notes on Numerical Fluid Mechanics and Multidisciplinary Design*, Springer International Publishing, 2016, pp. 177–187. https://doi.org/10.1007/978-3-319-27279-5_16, URL https://doi.org/10.1007/978-3-319-27279-5_16.

[3] Knopp, T., Reuther, N., Novara, M., Schanz, D., Schülein, E., Schröder, A., and Kähler, C., "Experimental analysis of the log law at adverse pressure gradient," *Journal of Fluid Mechanics*, Vol. 918, 2021. https://doi.org/10.1017/jfm.2021.331, URL https://doi.org/10.1017/jfm.2021.331.

[4] Schatzman, D. M., and Thomas, F. O., "An experimental investigation of an unsteady adverse pressure gradient turbulent boundary layer: embedded shear layer scaling," *Journal of Fluid Mechanics*, Vol. 815, 2017, pp. 592–642. https://doi.org/10.1017/jfm.2017.65, URL https://doi.org/10.1017/jfm.2017.65.

[5] Cary, A. W., Chawner, J., Duque, E. P., Gropp, W., Kleb, W. L., Kolonay, R. M., Nielsen, E., and Smith, B., "CFD Vision 2030 Road Map: Progress and Perspectives," *AIAA AVIATION 2021 FORUM*, American Institute of Aeronautics and Astronautics, 2021. https://doi.org/10.2514/6.2021-2726, URL https://doi.org/10.2514/6.2021-2726.

[6] Tinoco, E. N., Brodersen, O. P., Keye, S., Laflin, K. R., Feltrop, E., Vassberg, J. C., Mani, M., Rider, B., Wahls, R. A., Morrison, J. H., Hue, D., Roy, C. J., Mavriplis, D. J., and Murayama, M., "Summary Data from the Sixth AIAA CFD Drag Prediction Workshop: CRM Cases," *Journal of Aircraft*, Vol. 55, No. 4, 2018, pp. 1352–1379. https://doi.org/10.2514/1.c034409, URL https://doi.org/10.2514/1.c034409.

[7] Beck, A., and Kurz, M., "A perspective on machine learning methods in turbulence modeling," *GAMM-Mitteilungen*, Vol. 44, No. 1, 2021. https://doi.org/10.1002/gamm.202100002, URL https://doi.org/10.1002/gamm.202100002.

[8] Duraisamy, K., Iaccarino, G., and Xiao, H., "Turbulence Modeling in the Age of Data," *Annual Review of Fluid Mechanics*, Vol. 51, No. 1, 2019, pp. 357–377. https://doi.org/10.1146/annurev-fluid-010518-040547, URL https://doi.org/10.1146/annurev-fluid-010518-040547.

[9] Duraisamy, K., Singh, A. P., and Pan, S., "Field Inversion and Machine Learning (FIML) for Turbulence Modeling," 2016.

[10] Parish, E. J., and Duraisamy, K., "A paradigm for data-driven predictive modeling using field inversion and machine learning," *Journal of Computational Physics*, Vol. 305, 2016, pp. 758–774. https://doi.org/10.1016/j.jcp.2015.11.012, URL https://doi.org/10.1016/j.jcp.2015.11.012.

Downloaded by Markus Ruetten on December 6, 2022 | http://arc.aiaa.org | DOI: 10.2514/6.2022-3337

[11] Ling, J., and Kurzawski, A., "Data-driven Adaptive Physics Modeling for Turbulence Simulations," *23rd AIAA Computational Fluid Dynamics Conference*, American Institute of Aeronautics and Astronautics, 2017. https://doi.org/10.2514/6.2017-3627, URL https://doi.org/10.2514/6.2017-3627.

[12] Ling, J., Kurzawski, A., and Templeton, J., "Reynolds averaged turbulence modelling using deep neural networks with embedded invariance," *Journal of Fluid Mechanics*, Vol. 807, 2016, pp. 155–166. https://doi.org/10.1017/jfm.2016.615, URL https://doi.org/10.1017/jfm.2016.615.

[13] Wu, J.-L., Xiao, H., and Paterson, E., "Physics-informed machine learning approach for augmenting turbulence models: A comprehensive framework," *Physical Review Fluids*, Vol. 3, No. 7, 2018. https://doi.org/10.1103/physrevfluids.3.074602, URL https://doi.org/10.1103/physrevfluids.3.074602.

[14] Weatheritt, J., and Sandberg, R., "A novel evolutionary algorithm applied to algebraic modifications of the RANS stress–strain relationship," *Journal of Computational Physics*, Vol. 325, 2016, pp. 22–37. https://doi.org/10.1016/j.jcp.2016.08.015, URL https://doi.org/10.1016/j.jcp.2016.08.015.

[15] Weatheritt, J., Sandberg, R. D., Ling, J., Saez, G., and Bodart, J., "A Comparative Study of Contrasting Machine Learning Frameworks Applied to RANS Modeling of Jets in Crossflow," *Volume 2B: Turbomachinery*, American Society of Mechanical Engineers, 2017. https://doi.org/10.1115/gt2017-63403, URL https://doi.org/10.1115/gt2017-63403.

[16] Weatheritt, J., and Sandberg, R., "The development of algebraic stress models using a novel evolutionary algorithm," *International Journal of Heat and Fluid Flow*, Vol. 68, 2017, pp. 298–318. https://doi.org/10.1016/j.ijheatfluidflow.2017.09.017, URL https://doi.org/10.1016/j.ijheatfluidflow.2017.09.017.

[17] Zhao, Y., Akolekar, H. D., Weatheritt, J., Michelassi, V., and Sandberg, R. D., "RANS Turbulence Model Development using CFD-Driven Machine Learning," 2019. https://doi.org/10.48550/ARXIV.1902.09075, URL https://arxiv.org/abs/1902.09075.

[18] Weatheritt, J., Zhao, Y., Sandberg, R. D., Mizukami, S., and Tanimoto, K., "Data-driven scalar-flux model development with application to jet in cross flow," *International Journal of Heat and Mass Transfer*, Vol. 147, 2020, p. 118931. https://doi.org/10.1016/j.ijheatmasstransfer.2019.118931, URL https://doi.org/10.1016/j.ijheatmasstransfer.2019.118931.

[19] Menter, F. R., "Two-equation eddy-viscosity turbulence models for engineering applications," *AIAA Journal*, Vol. 32, No. 8, 1994, pp. 1598–1605. https://doi.org/10.2514/3.12149, URL https://doi.org/10.2514/3.12149.

[20] Rotta, J., "Statistische Theorie nichthomogener Turbulenz," *Zeitschrift für Physik*, Vol. 129, No. 6, 1951, pp. 547–572. https://doi.org/10.1007/bf01330059, URL https://doi.org/10.1007/bf01330059.

[21] Eisfeld, B., and Rumsey, C. L., "Length-Scale Correction for Reynolds Stress Modeling," *AIAA Aviation 2019 Forum*, American Institute of Aeronautics and Astronautics, 2019. https://doi.org/10.2514/6.2019-2961, URL https://doi.org/10.2514/6.2019-2961.

[22] Rumsey, C. L., "Application of Reynolds Stress Models to Separated Aerodynamic Flows," *Springer Tracts in Mechanical Engineering*, Springer International Publishing, 2015, pp. 19–37. https://doi.org/10.1007/978-3-319-15639-2_2, URL https://doi.org/10.1007/978-3-319-15639-2_2.

[23] Gerolymos, G. A., and Vallet, I., "Influence of Pressure-Strain Closure on the Prediction of Separated Flows," *Springer Tracts in Mechanical Engineering*, Springer International Publishing, 2015, pp. 61–83. https://doi.org/10.1007/978-3-319-15639-2_4, URL https://doi.org/10.1007/978-3-319-15639-2_4.

[24] Wilcox, D., *Turbulence modeling for CFD*, DCW Industries, Inc, La Canada, CA, 1993.

[25] Eisfeld, B., "Steps towards a Reynolds Stress Model for the Prediction of Separated Flows," *STO-AVT-307 Symposium*, MP-AVT, Vol. 307, NATO-STO, 2019, pp. 9.1–9.10. URL https://elib.dlr.de/130800/.

[26] Cécora, R.-D., Radespiel, R., and Jakirlić, S., "Modeling of Reynolds-Stress Augmentation in Shear Layers with Strongly Curved Velocity Profiles," *Springer Tracts in Mechanical Engineering*, Springer International Publishing, 2015, pp. 85–101. https://doi.org/10.1007/978-3-319-15639-2_5, URL https://doi.org/10.1007/978-3-319-15639-2_5.

[27] Speziale, C. G., Sarkar, S., and Gatski, T. B., "Modelling the pressure–strain correlation of turbulence: an invariant dynamical systems approach," *Journal of Fluid Mechanics*, Vol. 227, 1991, pp. 245–272. https://doi.org/10.1017/s0022112091000101, URL https://doi.org/10.1017/s0022112091000101.

[28] Bentaleb, Y., Lardeau, S., and Leschziner, M. A., "Large-eddy simulation of turbulent boundary layer separation from a rounded step," *Journal of Turbulence*, Vol. 13, 2012, p. N4. https://doi.org/10.1080/14685248.2011.637923, URL https://doi.org/10.1080/14685248.2011.637923.

[29] Lardeau, S., and Leschziner, M. A., "The interaction of round synthetic jets with a turbulent boundary layer separating from a rounded ramp," *Journal of Fluid Mechanics*, Vol. 683, 2011, pp. 172–211. https://doi.org/10.1017/jfm.2011.258, URL https://doi.org/10.1017/jfm.2011.258.

[30] Ferreira, C., "Gene Expression Programming: A New Adaptive Algorithm for Solving Problems," *Complex Systems*, Vol. 13, No. 2, 2001, pp. 87, 129.

[31] Reissmann, M., Hasslberger, J., Sandberg, R. D., and Klein, M., "Application of Gene Expression Programming to a-posteriori LES modeling of a Taylor Green Vortex," *Journal of Computational Physics*, Vol. 424, 2021, p. 109859. https://doi.org/10.1016/j.jcp.2020.109859, URL https://doi.org/10.1016/j.jcp.2020.109859.

[32] Zhong, J., Feng, L., and Ong, Y.-S., "Gene Expression Programming: A Survey [Review Article]," *IEEE Computational Intelligence Magazine*, Vol. 12, No. 3, 2017, pp. 54–72. https://doi.org/10.1109/mci.2017.2708618, URL https://doi.org/10.1109/mci.2017.2708618.

[33] Wheatheritt, J., "The Development of Data Driven Approaches to Further Turbulence Closures," , nov 2015.

[34] Panda, J., "A review of pressure strain correlation modeling for Reynolds stress models," *Proceedings of the Institution of Mechanical Engineers, Part C: Journal of Mechanical Engineering Science*, Vol. 234, No. 8, 2019, pp. 1528–1544. https://doi.org/10.1177/0954406219893397, URL https://doi.org/10.1177/0954406219893397.

Downloaded by Markus Ruetten on December 6, 2022 | http://arc.aiaa.org | DOI: 10.2514/6.2022-3337

[35] Lumley, J. L., and Newman, G. R., "The return to isotropy of homogeneous turbulence," *Journal of Fluid Mechanics*, Vol. 82, No. 1, 1977, pp. 161–178. https://doi.org/10.1017/s0022112077000585, URL https://doi.org/10.1017/s0022112077000585.

[36] Johansson, A. V., and Hallbäck, M., "Modelling of rapid pressure—strain in Reynolds-stress closures," *Journal of Fluid Mechanics*, Vol. 269, 1994, pp. 143–168. https://doi.org/10.1017/s0022112094001515, URL https://doi.org/10.1017/s0022112094001515.

[37] Eisfeld, B., "The importance of turbulent equilibrium for Reynolds-stress modeling," *Physics of Fluids*, Vol. 34, No. 2, 2022, p. 025123. https://doi.org/10.1063/5.0081157, URL https://doi.org/10.1063/5.0081157.

[38] Jakirlić, S., and Maduta, R., ""Steady" RANS Modeling for Improved Prediction of Wall-Bounded Separation," *AIAA Journal*, Vol. 54, No. 5, 2016, pp. 1803–1809. https://doi.org/10.2514/1.j054399, URL https://doi.org/10.2514/1.j054399.

[39] Rumsey, C. L., and Jeyapaul, E., "Pressure-strain and near-wall modeling for two-dimensional separated flows," center for Turbulence Research Proceedings of the Summer Program, 2012.

[40] Menter, F. R., "Two-equation eddy-viscosity turbulence models for engineering applications," *AIAA Journal*, Vol. 32, 1994, pp. 1598–1605.

[41] Eisfeld, B., and Brodersen, O., "Advanced Turbulence Modelling and Stress Analysis for the DLR-F6 configuration," *23rd AIAA Applied Aerodynamics Conference*, American Institute of Aeronautics and Astronautics, 2005. https://doi.org/10.2514/6.2005-4727, URL https://doi.org/10.2514/6.2005-4727.

[42] Eisfeld, B., and Rumsey, C. L., "Length-Scale Correction for Reynolds-Stress Modeling," *AIAA Journal*, Vol. 58, No. 4, 2020, pp. 1518–1528. https://doi.org/10.2514/1.j058858, URL https://doi.org/10.2514/1.j058858.

[43] Schwamborn, D., Gerhold, T., and Heinrich, R., "THE DLR TAU-CODE: RECENT APPLICATIONS IN RESEARCH AND INDUSTRY," *ECCOMAS CFD 2006 CONFERENCE*, 2006. URL https://elib.dlr.de/22421/, auf CD.

[44] Bekemeyer, P., and et. al., "Data-Driven Aerodynamic Modeling Using the DLR SMARTy Toolbox," American Institute of Aeronautics and Astronautics, 2022.

[45] Rumsey, C. L., "LES: 2-D curved backward-facing step," , 2021. URL https://turbmodels.larc.nasa.gov/Other_LES_Data/curvedstep.html, last accessed: 24 April 2022.

[46] Rumsey, C. L., "2DZP: 2D Zero Pressure Gradient Flat Plate Verification Case," , 2021. URL https://turbmodels.larc.nasa.gov/flatplate.html, last accessed: 24 April 2022.

[47] Schlatter, P., and ÖrlÜ, R., "Assessment of direct numerical simulation data of turbulent boundary layers," *Journal of Fluid Mechanics*, Vol. 659, 2010, pp. 116–126. https://doi.org/10.1017/s0022112010003113, URL https://doi.org/10.1017%2Fs0022112010003113.

Downloaded by Markus Ruetten on December 6, 2022 | http://arc.aiaa.org | DOI: 10.2514/6.2022-3337

[48] Jakirlić, S., and Hanjalić, K., "A new approach to modelling near-wall turbulence energy and stress dissipation," *Journal of Fluid Mechanics*, Vol. 459, 2002, pp. 139–166. https://doi.org/10.1017/s0022112002007905, URL https://doi.org/10.1017%2Fs0022112002007905.

[49] Cécora, R.-D., Radespiel, R., Eisfeld, B., and Probst, A., "Differential Reynolds-Stress Modeling for Aeronautics," *AIAA Journal*, Vol. 53, No. 3, 2015, pp. 739–755. https://doi.org/10.2514/1.j053250, URL https://doi.org/10.2514%2F1.j053250.

[50] Bradshaw, P., and Ferriss, D. H., "Calculation of boundary-layer development using the turbulent energy equation: compressible flow on adiabatic walls," *Journal of Fluid Mechanics*, Vol. 46, No. 1, 1971, pp. 83–110. https://doi.org/10.1017/s0022112071000417, URL https://doi.org/10.1017%2Fs0022112071000417.

[51] Rumsey, C. L., "2DFDC: 2D Fully-Developed Channel Flow at High Reynolds Number Validation Case," , 2021. URL https://turbmodels.larc.nasa.gov/channelflow_val.html, last accessed: 24 April 2022.

[52] Marusic, I., Monty, J. P., Hultmark, M., and Smits, A. J., "On the logarithmic region in wall turbulence," *Journal of Fluid Mechanics*, Vol. 716, 2013. https://doi.org/10.1017/jfm.2012.511, URL https://doi.org/10.1017%2Fjfm.2012.511.

[53] Project-Website, "HiFi-TURB - high precision and fast calculation of relevant flow features," , 2019. URL https://www.dlr.de/as/en/desktopdefault.aspx/tabid-15896/25759_read-66210/.

[54] Disotell, K. J., and Rumsey, C. L., "Design of an Axisymmetric Afterbody Test Case for CFD Validation," *23rd AIAA Computational Fluid Dynamics Conference*, American Institute of Aeronautics and Astronautics, 2017. https://doi.org/10.2514/6.2017-3792, URL https://doi.org/10.2514/6.2017-3792.

[55] Alaya, E., Grabe, C., and Knopp, T., "Design of a parametrized numerical experiment for a 2D turbulent boundary layer flow with varying adverse pressure gradient and separation behaviour," 2021, IB number DLR-IB-AS-GO-2020-109. URL https://elib.dlr.de/145131/.

[56] Waschkowski, F., Zhao, Y., Sandberg, R., and Klewicki, J., "Multi-objective CFD-driven development of coupled turbulence closure models," *Journal of Computational Physics*, Vol. 452, 2022, p. 110922. https://doi.org/10.1016/j.jcp.2021.110922, URL https://doi.org/10.1016%2Fj.jcp.2021.110922.

[57] Rumsey, C. L., "Exp: NASA Juncture Flow (JF)," , 2022. URL https://turbmodels.larc.nasa.gov/Other_exp_Data/junctureflow_exp.html, last accessed: 24 April 2022.

Downloaded by Markus Ruetten on December 6, 2022 | http://arc.aiaa.org | DOI: 10.2514/6.2022-3337